



## Broadband nonvolatile photonic switching based on optical phase change materials: beyond the classical figure-of-merit

QIHANG ZHANG,<sup>1</sup> YIFEI ZHANG,<sup>1</sup> JUNYING LI,<sup>1</sup> RICHARD SOREF,<sup>2</sup> TIAN GU,<sup>1</sup> AND JUEJUN HU<sup>1,\*</sup>

<sup>1</sup>Department of Materials Science & Engineering, Massachusetts Institute of Technology, 77 Massachusetts Avenue, Cambridge, Massachusetts 02139, USA

<sup>2</sup>Department of Engineering, University of Massachusetts Boston, Boston, Massachusetts 02125, USA

\*Corresponding author: hujuejun@mit.edu

Received 31 October 2017; revised 18 November 2017; accepted 22 November 2017; posted 22 November 2017 (Doc. ID 312323); published 21 December 2017

**In this Letter, we propose a broadband, nonvolatile on-chip switch design in the telecommunication C-band with record low loss and crosstalk. The unprecedented device performance builds on: 1) a new optical phase change material (O-PCM)  $\text{Ge}_2\text{Sb}_2\text{Se}_4\text{Te}_1$  (GSST), which exhibits significantly reduced optical attenuation compared to traditional O-PCMs, and 2) a nonperturbative design that enables low-loss device operation beyond the classical figure-of-merit (FOM) limit. We further demonstrate that the 1-by-2 and 2-by-2 switches can serve as basic building blocks to construct nonblocking and nonvolatile on-chip switching fabric supporting arbitrary numbers of input and output ports.** © 2017 Optical Society of America

**OCIS codes:** (130.4815) Optical switching devices; (160.2900) Optical storage materials; (250.6715) Switching.

<https://doi.org/10.1364/OL.43.000094>

Optical switching, i.e., dynamic routing of light into different paths, is an essential function in a photonic integrated circuit. Current on-chip optical switches are commonly based on electro-optic or thermo-optic effects. Both effects produce small refractive index perturbations typically well below 0.01, resulting in devices with large footprint and increased energy consumption. This limitation can be circumvented by employing a resonator structure, albeit at the expense of device bandwidth [1]. Furthermore, both types of switching mechanisms are volatile, requiring continuous power supply to maintain the optical switching state.

In recent years, devices based on O-PCMs have emerged for on-chip switching and routing [2]. Unlike electro-optic or thermo-optic effects which are minuscule, phase transition in O-PCMs generates gigantic optical property modulation (e.g., index change  $>1$ ) conducive to compact device architectures. In addition, such phase changes can be nonvolatile, exemplified by the transition between amorphous (a-) and crystalline (c-) states in chalcogenides. This attribute enables self-holding or

latching capability to sustain the switches' optical states even in the absence of power input.

Despite these attractive features, the performances of existing PCM-based photonic switches are severely compromised by the high optical absorption in traditional O-PCMs. The two most commonly used O-PCMs,  $\text{VO}_2$  and  $\text{Ge}_2\text{Sb}_2\text{Te}_5$  (GST 225), both suffer from excessive optical losses even in their dielectric states. For instance, the extinction coefficient in a-GST (which has lower optical loss compared to its crystalline state) mounts to 0.12 at 1550 nm wavelength, corresponding to 42,000 dB/cm attenuation—unacceptably high to most guided-wave device applications.

The impact of loss on the performance of optical switches is customarily quantified using the material figure-of-merit:

$$\text{FOM} = \Delta n/k, \quad (1)$$

where  $\Delta n$  and  $k$  denote the refractive index change and extinction coefficient of the active material, respectively. This FOM is widely quoted to gauge the performance of active materials used in switches and modulators, and it has been established that the FOM quantitatively correlates with the insertion loss (IL) and contrast ratio in all-optical, electro-optical, and magneto-optical devices [3–7]. Following this definition, classical O-PCMs are invariably plagued with low FOMs: e.g., the FOMs for  $\text{VO}_2$  and GST are approximately 0.7 and 2.1, respectively, at 1550 nm wavelength [8,9]. Consequently, switches based on the materials, whether theoretically analyzed [10,11] or experimentally implemented [12–14], exhibit unoptimized performance with high ILs of 2 dB or more and limited crosstalk of less than 15 dB in the C-band. Reduced ILs of approximately 1 dB were theoretically projected at wavelengths above 2  $\mu\text{m}$  where GST's absorption diminishes [11,15,16].

Here we propose a solution to overcome the performance limitations of on-chip optical switching devices based on O-PCMs. Central to our approach are: 1) a low-loss O-PCM; and 2) a device design that breaks the classical FOM limit.

The new O-PCM, Ge-Sb-Se-Te or GSST, is derived from the conventional GST alloy by partially substituting Te with Se [17]. Figure 1 compares the optical constants of  $\text{Ge}_2\text{Sb}_2\text{Se}_4\text{Te}_1$

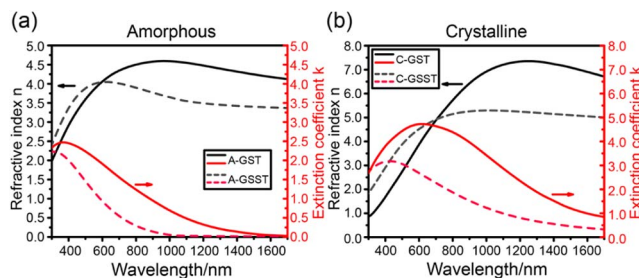


**Fig. 1.** Optical constants of (a) amorphous and (b) crystalline phases of  $\text{Ge}_2\text{Sb}_2\text{Te}_5$  (solid lines) and  $\text{Ge}_2\text{Sb}_2\text{Se}_4\text{Te}_1$  (dashed lines) from the visible range to near-infrared. The black lines represent the refractive index  $n$ , and the red curves are the extinction coefficient  $k$ .

with the classical GST 225 alloy, both of which were measured using ellipsometry on thermally evaporated films. We have also experimentally demonstrated reversible switching in GSST via laser or electrical pulsing, and the results will be summarized in a separate publication. From Fig. 1, it is evident that GSST exhibits reduced optical loss in both states compared to GST with an improved FOM of 4.2 at 1550 nm wavelength, twice that of GST. In particular, optical attenuation in a-GSST is vanishingly small in the telecom window, well below the sensitivity limit of ellipsometry. We therefore opted for a waveguide cut-back method to quantify the loss in a-GSST, which yields an extinction coefficient  $k = (1.8 \pm 1.2) \times 10^{-4}$ —over 600 times smaller than that of GST.

The FOM of GSST is predominantly limited by the moderate loss in its crystalline phase: at 1550 nm, c-GSST's extinction coefficient is 0.42, much lower than that of c-GST but still prohibitively high for guided-wave devices. The large loss contrast between the two phases in GSST prompted us to evaluate new designs to circumvent the high losses associated with the crystalline state. Close inspection of the FOM reveals that its derivation builds on a key underlying assumption: the material property modulation during the switching operation is sufficiently small such that perturbations to the optical mode comprise a high-order effect. Under this condition, the modal overlap with the active material can be characterized by a *single* parameter, i.e., the confinement factor  $\Gamma$ . Both the desired phase shift (induced by  $\Delta n$ ) and the unwanted optical loss (imposed by  $k$ ) scale with  $\Gamma$ , hence the FOM definition. The small perturbation assumption applies to devices relying on traditional electro-optic, thermo-optic, all-optical, and magneto-optical mechanisms, and therefore their performances are ultimately bound by the FOM, regardless of the specific device configuration—be it Mach-Zehnder interferometers (MZIs), directional couplers (DCs), or microring resonators [3,4]. The large optical property contrast between the two structural states in an O-PCM such as GSST, however, permits *different* modal confinement factors in the two states. For example, the device can be engineered to have large modal confinement within the GSST layer when it is in the low-loss amorphous state, and minimal optical field overlap with GSST when it is switched to the lossy crystalline phase. Such a “nonperturbative” design can be implemented to achieve low-loss, high-contrast switching beyond the classical performance limits set forth by the material FOM.

Figures 2(a) and 2(b) illustrate the mode profile modification in a GSST-loaded silicon nitride (SiN,  $n = 2.0$ ) waveguide,

simulated using the Lumerical Mode Solution package. In the crystalline phase, GSST has a sufficiently high index, and the c-GSST strip itself can support a tightly confined mode [Fig. 2(b)] with a large effective index of  $2.28 + 0.30i$ , whereas the mode in Fig. 2(a) spreads across both the a-GSST and SiN with a moderate effective index of  $1.68 + (2.1 \times 10^{-5})i$ . Clearly, the large modal modification cannot be accounted for using the classical perturbation theory.

Such a GSST-loaded waveguide is used as a basic component to construct advanced switching devices. The basic design rationale, following our preceding discussion on the limitations of the conventional FOM, is to engineer the light propagation path to allow input light to pass through the GSST when it is in the low-loss amorphous state, and divert light away from the lossy c-GSST leveraging the large mode modification induced by the GSST phase transition. As our first example, Figs. 2(c) and 2(d) plot the supermode profiles of two juxtaposed waveguides, a GSST-loaded SiN waveguide and a SiN waveguide without GSST. The waveguides have the same SiN core height, and their widths are adjusted such that their effective indices are identical when GSST is amorphous. Hence, phase matching leads to strong coupling between the two waveguides with well-defined even (symmetric) and odd (antisymmetric) supermodes [Fig. 2(c)]. In contrast, the large effective index disparity between the two guides in the crystalline state results in two isolated modes [Fig. 2(d)]. Figures 3(a) and 3(b) sketch a  $1 \times 2$  switch assuming a DC geometry based on the two-waveguide system. When GSST is amorphous, the phase matching condition between the two waveguides is met. Light launched into the input waveguide (the SiN waveguide without GSST strip) is therefore evanescently coupled and efficiently transferred into the other waveguide, as shown in the finite-difference time-domain (FDTD) modeled field profile in Fig. 3(c). Despite the large optical field overlap with GSST in this state, the low material attenuation in a-GSST facilitates low-loss operation. On the other hand, when the GSST film is crystallized, input light almost exclusively couples

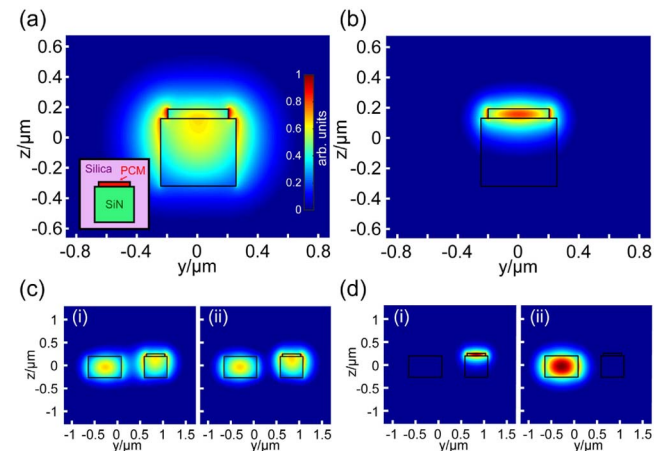


**Fig. 2.** (a), (b) Modal intensity profiles of a SiN waveguide loaded with a GSST strip in the (a) amorphous and (b) crystalline states. The inset in (a) illustrates the waveguide cross section; (c) intensity profiles of (i) even and (ii) odd supermodes in a two-waveguide system, one of which is topped with GSST while the other is not. The GSST layer is in (c) the amorphous state and (d) the crystalline state. All modes are TE-polarized.

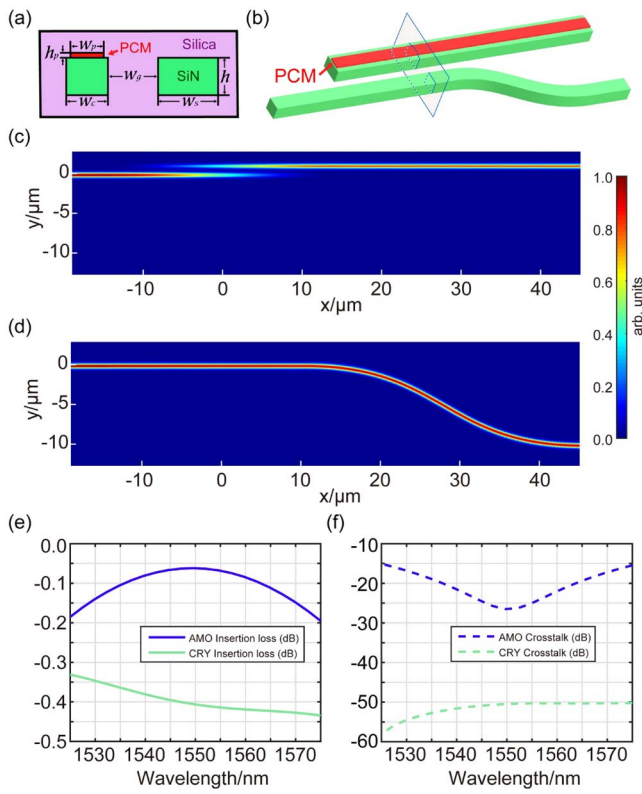


**Fig. 3.**  $1 \times 2$  switch: (a) cross-sectional structure of the  $1 \times 2$  switch. Here  $w_c = w_g = 500$  nm,  $w_s = 720$  nm,  $w_p = 400$  nm,  $h = 450$  nm, and  $h_p = 60$  nm; (b) schematic illustration of the  $1 \times 2$  switch, the rectangle marks the cross section depicted in (a); (c), (d) FDTD simulated optical field intensity distribution in the device at the (c) amorphous and (d) crystalline states; the simulations are performed using Lumerical FDTD Solutions; (e) insertion loss and (f) crosstalk of the switch across the telecom C-band. Here AMO and CRY stand for amorphous and crystalline states, respectively.

into the mode shown in Fig. 2(d) (ii) and remains in the input waveguide. The minimal optical field interaction with the lossy c-GSST layer ensures low insertion loss. The simulated IL and crosstalk (CT, i.e., contrast ratio between the on/off states at the output ports) are plotted in Figs. 3(e) and 3(f). At 1550 nm, the 40- $\mu\text{m}$ -long device attains an IL of 0.4 dB and a CT of over -50 dB for the crystalline state, and an IL as low as 0.06 dB and a CT of -27 dB in the amorphous state.

The “nonperturbative” design can be readily extended to  $2 \times 2$  switches. Figures 4(a) and 4(b) schematically depict the switch layout. We note that while similar three-waveguide DC designs have previously been proposed [10,11], they were based on traditional GST and therefore unable to exploit the advantages of the “nonperturbative” design (see Table 1). Figures 4(c) and 4(d) portray the FDTD-simulated field distributions in the  $2 \times 2$  device when the GSST strip is in the amorphous [Fig. 4(c)] and crystalline [Fig. 4(d)] states. The working principle of the device can be accounted for using the supermode theory, where the three supermodes of the three-waveguide section are approximated as linear combinations of the normalized individual waveguide modes (labeled from left to right as  $|1\rangle$ ,  $|2\rangle$  and  $|3\rangle$ ) as:  $\frac{1}{2}|1\rangle + \frac{\sqrt{2}}{2}|2\rangle + \frac{1}{2}|3\rangle$ ,  $\frac{\sqrt{2}}{2}|1\rangle - \frac{\sqrt{2}}{2}|3\rangle$ , and  $\frac{1}{2}|1\rangle - \frac{\sqrt{2}}{2}|2\rangle + \frac{1}{2}|3\rangle$ .

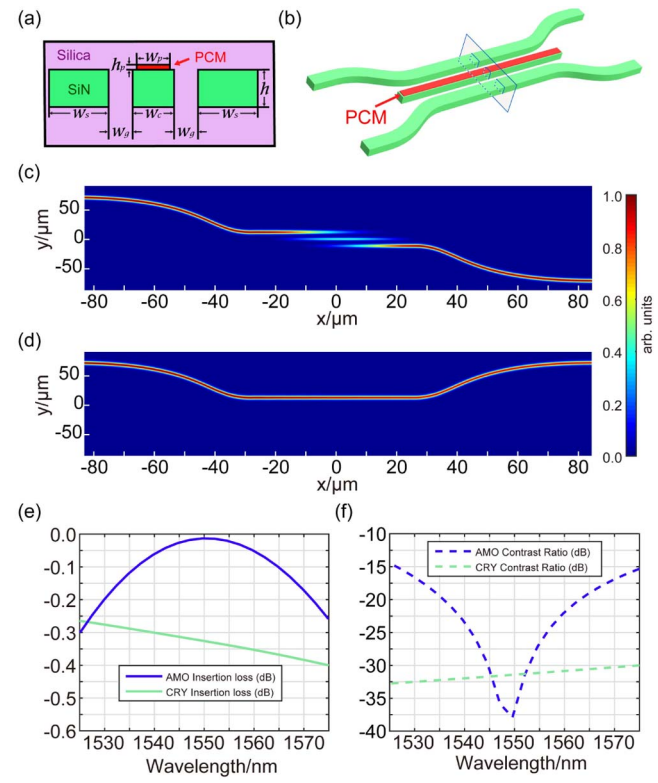


**Fig. 4.**  $2 \times 2$  switch: (a) cross section and (b) perspective view of the switch. Here  $w_c = 512$  nm,  $w_s = 730$  nm,  $w_p = 400$  nm,  $w_g = 562$  nm,  $h = 450$  nm, and  $h_p = 60$  nm; (c), (d) FDTD simulated field intensity distribution in the device at the (c) amorphous (cross) and (d) crystalline (bar) states; (e) insertion loss and (f) crosstalk of the switch across the telecom C-band.

It can be shown that complete power transfer (i.e., zero crosstalk) in the cross state [Fig. 4(c)] requires that the propagation constants of the three supermodes are evenly spaced, which approximately holds in our optimized design presented in Fig. 4. The design exhibits broadband switching capability across the C-band [Figs. 4(e) and 4(f)]. At 1550 nm, the ILs for the cross and bar states are 0.013 and 0.32 dB, and the CTs for the two states are -37 and -32 dB, respectively. These figures represent, to the best of our knowledge, the best performance for nonvolatile on-chip optical switches.

To elucidate the respective contributions to this exceptional performance from: 1) substitution of GST with GSST, and 2) the nonperturbative design, we modeled switches based on a GST alloy as well as a traditional MZI design. In the MZIs, one of the interferometer arms is loaded with a thin layer of O-PCM to induce  $\pi$  phase shift upon crystallization. The power splitting ratios in the arms are chosen to balance the

**Table 1. Performance Comparison between Different  $2 \times 2$  Switch Designs**

	Traditional MZI		Nonperturbative Design	
	GST	GSST	GST	GSST
IL (dB)	8.6	3.5	2.5	0.32
CT (dB)	-0.02	-6.1	-20	-32

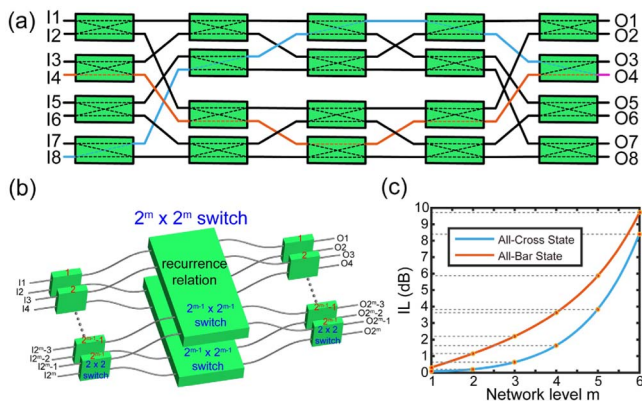


**Fig. 5.**  $2^m \times 2^m$  Benes network based on the nonvolatile switch: (a) network topology of a  $8 \times 8$  switch ( $m = 3$ ); (b) schematic diagram illustrating the recurrence relation between a  $2^m \times 2^m$  switch and  $2^{m-1} \times 2^{m-1}$  switch: a level- $m$  switch comprises two level- $(m-1)$  switches and  $2^{m-1} \times 2^{m-1}$  switches; (c) insertion losses of the switch at 1550 nm. The all-cross state corresponds to  $I2^{m-1}-O2^{m-1}$  [marked with blue color in (a) for the  $8 \times 8$  case]. The all-bar state is the  $I2^{m-1}-O2^{m-1}$  path [marked with orange color in (a)].

MZI arms when the O-PCM is in the amorphous state, which maximizes the CT. However, when the O-PCM is crystallized, its increased absorption results in power imbalance between the arms, compromising both the CT and IL. It can be shown that performance of MZI switches is defined by the classical FOM [3,4]. Results in Table 1, which indicate that only the combination of the GSST material and the nonperturbative design reaches the performance target, highlight the critical importance of both material innovation and device engineering.

Finally, we use the  $2 \times 2$  switch as a building block to assemble a Benes network, a nonblocking switching fabric architecture that can be scaled to realize arbitrary network complexity levels. As an example, Fig. 5(a) depicts the block diagram for an  $8 \times 8$  switch, and Fig. 5(b) illustrates the generic scaling law to construct a  $2^m \times 2^m$  switch. Generally, a  $2^m \times 2^m$  switch consists of  $2^{m-1}$  rows and  $2^{m-1}$  columns of  $2 \times 2$  switches. Therefore, light always passes through a total of  $2^{m-1} 2 \times 2$  switches in the fabric. To compute the IL of the entire network, we consider ILs from individual  $2 \times 2$  switches on the optical path as well as loss due to waveguide crossings. The IL of a waveguide crossing is taken as 0.1 dB, which has been experimentally realized in the C-band [18]. Because the  $2 \times 2$  switch element has higher IL in the bar state [Fig. 4(e)], the ILs of all-bar and all-cross states approximately correspond to the upper and lower bounds of the network IL. For the all-bar state,  $I2^{m-1}-O2^{m-1}$  [highlighted in orange in Fig. 5(a)] represents a lossy path with a large number of crossings. The IL for this path is:

$$(2^m - 2) \times 0.1 \text{ dB} + 2m - 1 \times 0.32 \text{ dB}. \quad (2)$$

An exemplary all-cross state path is  $I2^m-O2^{m-1}$  [highlighted with blue color in Fig. 5(a)]. The corresponding IL is:

$$(3 \times 2^{m-1} - 1 - 2m) \times 0.1 \text{ dB} + (2m - 1) \times 0.013 \text{ dB}, \quad (3)$$

dominated by the waveguide crossing loss. The CT, defined as the ratio of transmitted power from the target output port over the maximum leaked power from a “nontarget” port, is estimated using the following formula at 1550 nm for a  $2^m \times 2^m$  switch:

$$-(32 \text{ dB} - 10 \cdot \log_{10} m \text{ dB}), \quad (4)$$

where  $-32$  dB is the “worst-case” (bar state) CT for a  $2 \times 2$  switch, and the second factor adds up leaked power from each switch stage. Figure 5(c) plots the all-bar and all-cross ILs versus the network level  $m$  following Eqs. (2) and (3). In a  $16 \times 16$  switch, the ILs for all-cross and all-bar states are 1.6 and 3.6 dB, respectively, and the ILs in a  $32 \times 32$  switch are 3.9 and 5.9 dB. The CTs for a  $16 \times 16$  switch and a  $32 \times 32$  switch are  $-26$  and  $-25$  dB, respectively. These figures represent a significant improvement compared to state-of-the-art (volatile) on-chip switches (e.g., for  $16 \times 16$  switches, the reported ILs are 6.7 and 14 dB, and the CT is  $-15.1$  dB [19]. The corresponding ILs are 12.9 and 16.5 dB in  $32 \times 32$  switches, and the CT is approximately  $-15$  dB [18]).

We propose and model nonvolatile optical switches based on O-PCMs. Through combining low-loss phase change alloys and a “nonperturbative” design, the switches demonstrate significantly enhanced performances compared to current state-of-the-art. Across the telecom C-band, individual  $1 \times 2$  and  $2 \times 2$  switches exhibit ILs between 0.01 to 0.4 dB, and CTs consistently above 15 dB ( $>25$  dB at 1550 nm). We show that the technology can be scaled to realized nonblocking matrix switches with arbitrary network complexity. The low-loss, nonvolatile switching technology, once materialized, will find numerous applications for optical communications, optical signal processing, and field-programmable reconfigurable photonics.

**Funding.** Defense Advanced Research Projects Agency (DARPA) (Extreme Optics and Imaging (EXTREME)).

## REFERENCES

1. H. Lin, O. Ogbuu, J. Liu, L. Zhang, J. Michel, and J. Hu, *J. Lightwave Technol.* **31**, 4029 (2013).
2. M. Wuttig, H. Bhaskaran, and T. Taubner, *Nat. Photonics* **11**, 465 (2017).
3. R. A. Soref, D. McDaniel, and B. R. Bennett, *J. Lightwave Technol.* **6**, 437 (1988).
4. X. Y. Sun, Q. Du, T. Goto, M. C. Onbasli, D. H. Kim, N. M. Aimon, J. Hu, and C. A. Ross, *ACS Photon.* **2**, 856 (2015).
5. A. Astill, *Thin Solid Films* **204**, 1 (1991).
6. M. Nedeljkovic, R. Soref, and G. Z. Mashanovich, *IEEE Photon. J.* **7**, 1 (2015).
7. L. Bi, J. Hu, P. Jiang, H. S. Kim, D. H. Kim, M. C. Onbasli, G. F. Dionne, and C. A. Ross, *Materials* **6**, 5094 (2013).
8. H. W. Verleur, A. Barker, Jr., and C. Berglund, *Phys. Rev.* **172**, 788 (1968).
9. B.-S. Lee, J. R. Abelson, S. G. Bishop, D.-H. Kang, B.-K. Cheong, and K.-B. Kim, *J. Appl. Phys.* **97**, 093509 (2005).
10. Y. Ikuma, T. Saiki, and H. Tsuda, *IEICE Electron. Express* **5**, 442 (2008).
11. H. Liang, R. Soref, J. Mu, A. Majumdar, X. Li, and W.-P. Huang, *J. Lightwave Technol.* **33**, 1805 (2015).
12. M. Rudé, J. Pello, R. E. Simpson, J. Osmond, G. Roelkens, J. J. van der Tol, and V. Pruneri, *Appl. Phys. Lett.* **103**, 141119 (2013).
13. M. Stegmaier, C. Ríos, H. Bhaskaran, C. D. Wright, and W. H. Pernice, *Adv. Opt. Mater.* **5**, 1600346 (2017).
14. T. Moriyama, D. Tanaka, P. Jain, H. Kawashima, M. Kuwahara, X. Wang, and H. Tsuda, *IEICE Electron. Express* **11**, 20140538 (2014).
15. H. Liang, R. Soref, J. Mu, X. Li, and W.-P. Huang, *Appl. Opt.* **54**, 5897 (2015).
16. B. Ma, P. Zhang, H. Wang, T. Zhang, J. Zeng, Q. Zhang, G. Wang, P. Xu, W. Zhang, and S. Dai, *Appl. Opt.* **55**, 9205 (2016).
17. Y. Zhang, J. Li, J. Chou, Z. Fang, A. Yadav, H. Lin, Q. Du, J. Michon, Z. Han, and Y. Huang, *Conference on Lasers and Electro-Optics (CLEO)* (Optical Society of America, 2017), paper JTh5C.4.
18. L. Qiao, W. Tang, and T. Chu, *Sci. Rep.* **7**, 42306 (2017).
19. L. Lu, S. Zhao, L. Zhou, D. Li, Z. Li, M. Wang, X. Li, and J. Chen, *Opt. Express* **24**, 9295 (2016).